Optimal Phase-Shift Control to Minimize Reactive Power for a Dual Active Bridge DC–DC Converter

Shuai Shao, *Member, IEEE*, Mingming Jiang, Weiwen Ye, Yucen Li, Junming Zhang, *Senior Member, IEEE*, and Kuang Sheng, *Senior Member, IEEE*

***Abstract*—In a dual active bridge (DAB) dc–dc converter, modulating the phase-shift ratios can suppress reactive power and increase the efficiency under non-unity voltage gain conditions. Derivation of the optimal phase-shift ratios to achieve the minimum reactive power is challenging because a DAB can operate in four different scenarios (forward/backward, buck/boost) and each scenario has five operating modes. This paper first introduces a transformation in which different DAB operating scenarios (forward/backward, buck/boost) can be equivalent to one another; then optimization of only one scenario (forward/buck) is required. Next, for the five modes in forward/buck scenario, based on a graphical method, this paper proves that each operating point of Modes 1, 2, and 5 can be mapped into that of Mode 3 with lower conduction losses, and only two modes require detailed analysis. The optimization process of these two modes are derived step-by-step. Global optimal phase-shift signals that minimize the reactive power under four different DAB operating scenarios (forward/backward, buck/boost) are presented. A simple table and control block diagram are presented for practical implementation of global reactive-power minimization control. Experimental comparison with other modulation schemes verifies the efficiency improvement of the proposed control method.**

***Index Terms*—DC–DC converter, dual active bridge (DAB), phase shift, reactive-power suppression.**

I. Introduction

THE dual active bridge (DAB), first proposed by Doncker *et al.* [1] and [2] in 1988, is a galvanic-isolated, bi-directional dc–dc converter. As shown in Fig. 1(a), a typical DAB consists of a transformer, and two H-bridges located on the primary and secondary sides of the transformer. Each power device switches with 50% duty cycle and two square voltages, v_{ab} and v_{cd}, can be generated. The transformer provides isolation and voltage matching between the two H-bridges. The transformer leakage inductance (or an additional inductor) serves as the instantaneous energy storage element. Operation is bi-directional, and either H-bridge can be considered the primary or secondary depending on the power-flow direction [3]. A DAB can be simplified, as in Fig. 1(b), assuming ideal power semiconductor devices and transformer. The parameters definitions are presented in Table I.

Manuscript received September 6, 2018; revised November 8, 2018; accepted December 20, 2018. Date of publication January 1, 2019; date of current version June 28, 2019. This work was supported in part by Lite-On Power Electronics Technology Research Fund, in part by the National Natural Science Foundation of China under Grant 51607156, and in part by the Public Welfare Research Projects of Zhejiang Province under Grant 2017C31001. Recommended for publication by Associate Editor J. Biela. *(Corresponding author: Shuai Shao.)*

The authors are with the College of Electrical Engineering, Zhejiang University, Hangzhou 310027, China (e-mail:

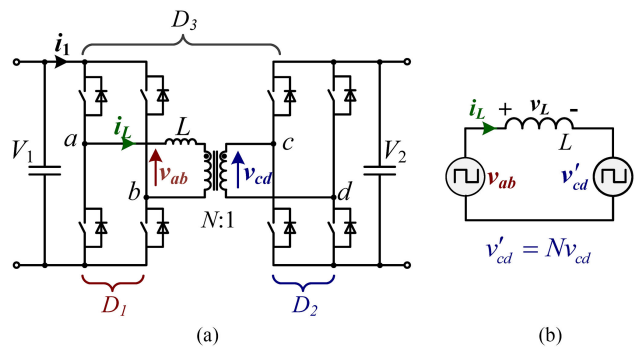

Parameters	Definition
V_1, V_2	DC voltage of primary and secondary side voltage respectively
v_{ab}, v_{cd}	Square voltage generated by primary and secondary side H-bridges
v'_{cd}	Reflected v_{cd} from secondary to primary side, $v'_{cd} = Nv_{cd}$
D_1, D_2	Duty cycle of v_{ab} and v_{cd} respectively (see Fig. 2), $D_1, D_2 \in (0, 1]$
D_3	Phase shift between v_{ab} and v_{cd} (see Fig. 2), $D_3 \in [-0.5, 0.5]$
D_f	Phase shift between v_{ab} and v_{cd} fundamental components (see Fig. 5), $D_f \in [-0.5, 0.5]$
T_s	DAB switching cycle (see Fig. 2)
T_h	Half a switching cycle, $T_h = T_s/2$ (see Fig. 2)
d	Voltage gain, $d = NV_2/V_1$. $d < 1$, buck mode; $d > 1$, boost mode.
P	$P > 0$, forward (left to right); $P < 0$, backward.
P_n	Nominal output power (see Eq. (11))

DAB is ideal for energy storage systems (ESSs) and power electronic transformers (PETs) because of the following features.

1) *Automatic seamless bi-directional power flow:* It is ideal for PETs and ESSs in microgrids that require fast power-flow direction transition.
2) *Wide voltage conversion gain range:* It is ideal for interfacing ESSs such as batteries or super-capacitors, whose voltages vary significantly under different state of charge.
3) *Zero voltage switching (ZVS)-ON capability with proper control*: It is ideal to be able to achieve high efficiency.

See http://www.ieee.org/publications_standards/publications/rights/index.html for more information.

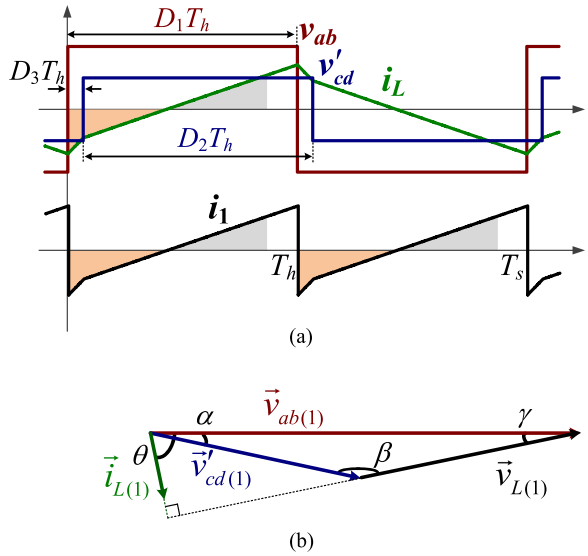

Fig. 2. (a) Typical waveforms of a DAB converter using SPS with $d = 0.4$, and (b) the corresponding phasor diagram (fundamental components).

Despite aforementioned desirable features, a DAB suffers from the reactive-power problem (also called circulating current). Conventionally, a DAB is modulated using single phase shift (SPS) modulation, and the reactive power can decrease the efficiency significantly when the voltage gain is not unity. Fig. 2(a) shows typical waveforms when using SPS modulation, in which $D_1 = D_2 = 1$; only D_3 is manipulated to regulate the output voltage. In the case of Fig. 2(a) where the voltage gain $d = NV_2/V_1 = 0.4$, the inductor current i_L involves a large portion of reverse current (orange shaded area) that transmits power backward, and i_L has to increase its forwarding part (gray shaded area) to compensate for the reverse portion as illustrated in Fig. 2(a). The orange- and gray-shaded portion currents are called reactive currents in a DAB. Similar to the one in power system, the reactive power does not transfer any energy, but produces conduction losses in power devices and copper loss in transformer.

The amount of DAB reactive power increases as the voltage gain moves away from unity. This phenomenon can be explained using the phasor diagram [2], [4] in Fig. 2(b). These phasors satisfy

$$\begin{cases} \vec{v}_{L(1)} = \vec{v}_{ab(1)} - \vec{v}'_{cd(1)} \\ \vec{i}_{L(1)} = \vec{v}_{L(1)}/j\omega L. \end{cases} \tag{1}$$

The angles between these phasors satisfy the law of sines as follows:

$$\begin{cases} \beta + \gamma = \pi - \alpha \\ \dfrac{\sin\gamma}{\sin\beta} = \dfrac{|\vec{v}'_{cd(1)}|}{|\vec{v}_{ab(1)}|} = d \\ \theta = \dfrac{\pi}{2} - \gamma. \end{cases} \tag{2}$$

For a given α ($\alpha = D_3\pi$), a small d leads to a small γ and large θ according to (2) and Fig. 2(b) when $d < 1$. A large θ [the angle between $\vec{v}_{ab(1)}$ and $\vec{i}_{L(1)}$] results in a high percentage of the reactive power. The reactive power will increase further as d decreases.

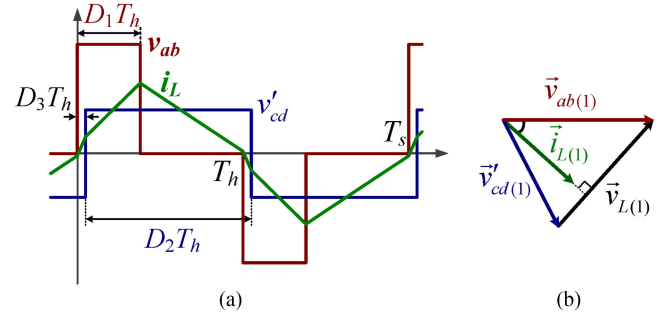

Fig. 3. (a) Waveforms of a DAB converter with an adjusted D_1, and (b) the corresponding phasor diagram (fundamental components).

An intuitive way to suppress the reactive power is to adjust the duty ratios of $\vec{v}_{ab(1)}$ and $\vec{v}'_{cd(1)}$, such that amplitudes of $\vec{v}_{ab(1)}$ and $\vec{v}'_{cd(1)}$ are similar. v_{ab} can be expressed using Fourier series

$$|\vec{v}_{ab(n)}| = \frac{4\sin(n\pi/2)\sin(D_1 n\pi/2)}{n\pi} V_1, n = 1, 3, 5, \ldots \tag{3}$$

where $|\vec{v}_{ab(n)}|$ denotes the amplitude of different frequency component. Decreasing D_1 can reduce amplitude $\vec{v}_{ab(1)}$ as shown in Fig. 3. With a smaller D_1, the angle between $\vec{v}_{ab(1)}$ and $\vec{i}_{L(1)}$ in Fig. 3(b) becomes smaller compared with Fig. 2(b), and the reactive power of Fig. 3(a) is reduced. The phase-shift ratios can be adjusted further to reduce the reactive power, and how to choose proper values of D_1, D_2, and D_3 to minimize the reactive power is an active topic of research on DAB [5]–[20].

Based on the phase-shift ratios (D_1, D_2, and D_3) that are manipulated, the modulation methods can be classified as follows.

1) SPS: $D_1 = D_2 = 1$, and only D_3 is controlled for output voltage regulation.
2) Dual phase shift (DPS): Besides D_3, another degree of freedom is introduced to suppress the circulating current, and there are two possible ways, the first way is to regulate D_1 or D_2 depending on the voltage gain M [5]–[8], and the second way is to regulate both D_1 and D_2, but let $D_1 = D_2$ [9]–[12].
3) Triple phase shift (TPS): D_1, D_2, and D_3 are controlled independently [13]–[20].

Although the DPS can reduce DAB reactive power to some extent, yet their phase-shift ratios (D_1, D_2, and D_3) are only locally optimized [18]. This is also the case for preliminary TPS methods including triangular and trapezoidal modulation methods, whose name comes from the shape of the inductor current [21]–[23].

With different operating modes and three degrees of freedom, it is challenging to obtain the global optimal parameters for a DAB. The first way is to approximate square voltages and inductor currents using fundamental components [13]–[15]. The optimal values of D_1, D_2, and D_3 are obtained by maximizing fundamental power factor [13], minimizing the amplitudes of

the fundamental components of i_L [14], or minimizing the fundamental reactive power [15]. The derivation process of these methods is straightforward; however, fundamental-component approximation of the square voltages introduces error, especially, when either D_1 or D_2 is close to 0, in which case the fundamental frequency component of v_{ab} (or v_{cd}) is not the dominant frequency component any more according to (3).

In the time domain, to derive the global optimal values of D_1, D_2, and D_3 in TPS, different operating modes have to be considered because the expressions of current and power are different for each mode. Krismer *et al.* [16] has classified DAB operation into 12 different modes, but some of those modes are not allowed in practice to ensure monotonicity between output power and phase shift. Jain *et al.* [17] has simplified DAB operation (buck/forward) into five different operating modes and obtained the optimal values of D_1, D_2, and D_3, but the derivation process is insufficient. On the basis of the mode classification in [17], Huang *et al.* [18] rigorously derived the global optimal values of D_1, D_2, and D_3 using the Karush–Kuhn–Tucker (KKT) method and numerical comparisons. Hou *et al.* [19] also deduced the optimal values of D_1, D_2, and D_3 using the Lagrange multiplier method (LMM), though some of the operating modes are not considered. Tong *et al.* [20] pointed out that the LMM used in [18] and [19] (the KKT method is also an LMM method) lacks sufficiency because of non-convex feasible region in some of the operating modes. The optimal values of D_1, D_2, and D_3 in [20] were derived on the basis of the minimized RMS value of inductor current i_L, and the resultant optimal parameters are the same as in [18] and [19]. Although the global optimal values of D_1, D_2, and D_3 have been found in [18]–[20], yet the derivation processes are complicated because of extensive optimization for each mode. Besides, the negative output power condition is not considered in these aforementioned papers.

This paper simplifies the derivation of the optimal phase-shift ratios to minimize DAB reactive power compared to [18]–[20]. First, we introduce a transformation that different DAB operating scenarios (forward/backward, buck/boost) can be equivalent to one another; then, only optimization of one scenario (forward/buck) is required, and optimal phase-shift ratios of other scenarios can be obtained using this equivalence. For the forward/buck scenario, there are five different operating modes (Modes 1–5). Employing a graphical method, this paper proves that each operating point of Modes 1, 2, and 5 can be mapped into that of Mode 3 with lower conduction losses, and that only two modes require consideration. The optimization process of these two modes is derived in a step-by-step manner. These equivalences not only simplify the calculation but also provide a better understanding of the operating principle of a DAB. Global optimal phase-shift signals that minimize the reactive power under four different DAB operating scenarios (forward/backward, buck/boost) are presented. A table and control block diagram are presented for practical implementation of global reactive-power minimization control. Experimental results are obtained under various voltage and load conditions to validate the proposed control scheme.

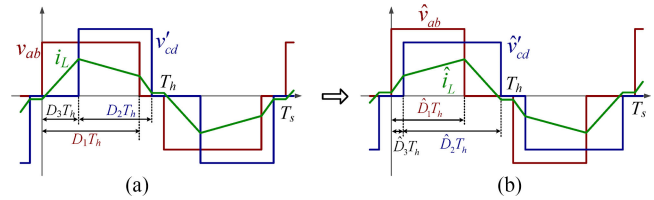

Fig. 4. Symmetrical transformation from forward/boost to forward/buck scenarios.

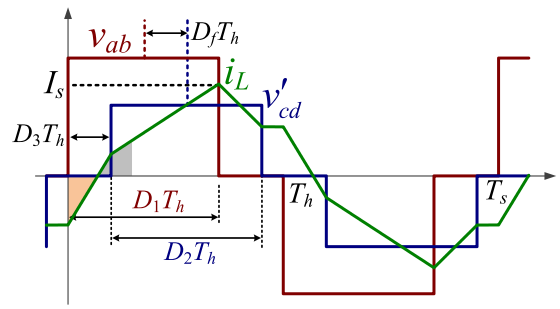

Fig. 5. Generic waveforms of a DAB.

II. Equivalence of Different Scenarios

Depending on the power (P) flow direction and voltage gain d, a DAB can operate in the following four different scenarios:

1) forward/buck ($P > 0,\ d < 1$);
2) forward/boost($P > 0,\ d > 1$);
3) backward/buck ($P < 0,\ d < 1$);
4) backward/boost ($P < 0,\ d > 1$).

It is possible to transform Scenarios 2)–4) to 1) to simplify the analysis.

Consider the forward/boost case whose typical waveforms are shown in Fig. 4(a). We can construct a forward/buck scenario shown in Fig. 4(b) with the following parameters:

$$\begin{cases} \hat{d} = 1/d \\ \hat{v}_{ab} = v'_{cd} \\ \hat{v}'_{cd} = v_{ab} \\ \hat{D}_1 = D_2 \\ \hat{D}_2 = D_1 \\ \hat{D}_3 = D_2 + D_3 - D_1. \end{cases} \tag{4}$$

The square voltages and inductor currents of Fig. 4(a) and (b) are mirror-symmetrical to each other, with the exact same output power and circulating power. Similar transformation can also be performed for Scenarios 3) and 4). Therefore, only the forward/buck case requires a detailed analysis to obtain the minimal reactive-power conditions, and the optimal conditions of other scenarios can be derived using this simple equivalence.

III. Operating Modes in Forward/Buck Case

Fig. 5 shows generic waveforms of a DAB in forward/buck case, where the parameters are presented in Table I. D_f is the phase shift between the fundamental components of v_{ab} and

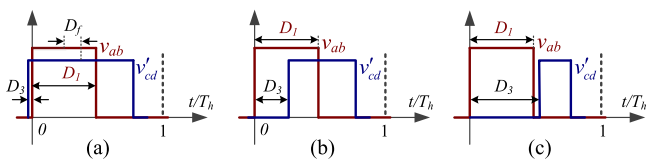

Fig. 6. Mode 1, Modes 2–4, and Mode 5 are differentiated by the rising edge position of v'_{cd} (t/T_h is the horizontal axis).

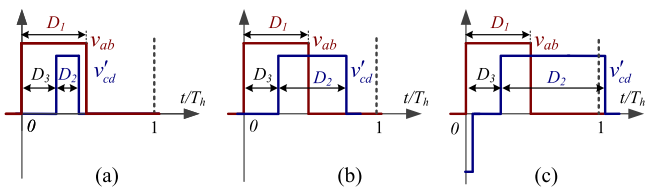

Fig. 7. Modes 2–4 are differentiated by the falling edge position of v'_{cd} (t/T_h is the horizontal axis).

v_{cd} [13], [18], and can be expressed as:

$$D_f = \frac{D_2}{2} - \frac{D_1}{2} + D_3. \tag{5}$$

According to [13] and [18], the output power can be expressed using Fourier series:

$$P = \sum_{k=1,3,5,\ldots} \frac{4NV_1V_2T_s \sin\alpha \sin\beta \sin\gamma}{(k\pi)^3 L} \tag{6}$$

where $\alpha = kD_1\pi/2$, $\beta = kD_2\pi/2$, and $\gamma = kD_f\pi$. According to (6), D_f must in range of $[-1/2, 1/2]$ to ensure monotonicity between P and D_f.

For the forward/buck scenario ($P > 0, d < 1$), the constraints on D_1, D_2 and D_f are: $D_1, D_2 \in (0, 1]$ and $D_f \in (0, 1/2]$. Then, on the basis of the relative positions of v_{ab} and v'_{cd}, there are only five possible operating modes, as shown in Figs. 6 and 7. For a given v_{ab}, the rising edge of v'_{cd} can only be in the following three possible positions:

1) Mode 1 [see Fig. 6(a)]: The rising edge of v'_{cd} leads that of v_{ab}, where $D_3 \leq 0$. On the basis of the constraint $D_f > 0$, we derive $D_2 + D_3 > D_1$ according to (5), which means the falling edge of v'_{cd} must lag that of v_{ab}.
2) Modes 2–4 [see Fig. 6(b)]: The rising edge of v'_{cd} is located between the rising and fall edges of v_{ab}, where $0 \leq D_3 \leq D_1$.
3) Mode 5 [see Fig. 6(c)]: The rising edge of v'_{cd} lags behind the falling edge of v_{ab}, where $D_3 \geq D_1$. On the basis of the constraint $D_f \leq 1/2$, we derive $D_2 + D_3 \leq 1$ according to (5), which means the falling edge of v'_{cd} is within the same half cycle as its rising edge.

The difference between Modes 2, 3, and 4 is the position of the falling edge of v'_{cd} (determined by $D_2 + D_3$), as shown in Fig. 7:

1) Mode 2 [see Fig. 7(a)]: The falling edge of v'_{cd} is ahead of the falling edge of v_{ab}, i.e., $D_2 + D_3 \leq D_1$.
2) Mode 3 [see Fig. 7(b)]: The falling edge of v'_{cd} lags behind that of v_{ab}, and is within the first half cycle, i.e., $D_1 \leq D_2 + D_3 \leq 1$.
3) Mode 4 [see Fig. 7(c)]: The falling edge of v'_{cd} is located at the second half cycle, i.e., $D_2 + D_3 \geq 1$.

On the basis of the aforementioned analysis, Fig. 8 summarizes the five different modes when a DAB operates in buck/forward scenario. In the next section, we will simplify the analysis by proving that the minimal reactive-power points must lie in Modes 3 and 4.

Before proceeding, it is necessary to choose a proper variable to indicate the amount of reactive power. In literature, the reactive power has been indicated using total power losses [7], [11], reverse power [8], [17], RMS value of i_L [20], [23], and current stress (peak current) of i_L [8], [12], [18], [19]. Among these variables, the RMS value minimization is the most reasonable target because the conduction losses of power devices, inductor and transformers are proportional to this value. However, the RMS value itself requires an intensive calculation, which will complicate the optimization. A simpler and effective way is the current stress of i_L, i.e., I_s shown in Fig. 5. For the same output power, increment in the reactive power (orange area of Fig. 5) will increase the current stress of i_L. In this paper, the inductor-current stress is used to indicate the reactive power, and the aim of this paper is to obtain the optimal combination of the values of D_1, D_2, and D_3 for given P and d such that current stress of inductor current i_L is minimum.

IV. Modes 1, 2, and 5

In this section, on the basis of a graphical method, we will prove that each operating point of Modes 1, 2, and 5 can be mapped into that of Mode 3 with lower conduction losses.

Mode 2 ($D_3 \geq 0, D_2 + D_3 \leq D_1$) is considered first. As shown in Fig. 9, for any operating point in Mode 2, shrink of v_{ab} at the rising and falling edges with a period $(D_1 - D_2 - D_3)T_h$ can let the DAB operate in Mode 3. This transformation does not change the output power because the gray areas of i_L in Fig. 9(a) and (b) are exactly the same. Meanwhile, the RMS value of i_L in Fig. 9(b) is reduced. For any operating point in Mode 2, there always exists a corresponding point in Mode 3 with the same output power and current stress, but with lower power losses. A similar equivalence can be established for Mode 5 by reducing D_3 by $D_1 - D_3$ as shown in Fig. 10. Thus, no further analysis is required for Modes 2 and 5.

For Mode 1, there are three possible cases: 1) $i_L(0) > 0$; 2) $i_L(0) = 0$; and 3) $i_L(0) < 0$, as shown in Fig. 11, where $i_L(0)$ represents the i_L value at the time 0. In this mode, the DAB output power can be expressed as:

$$P = \frac{1}{T_h}\int_0^{T_h} (v_{ab} \cdot i_L)dt = \frac{V_1}{T_h}\int_0^{D_1T_h} i_L dt \tag{7}$$

where $T_h = T_s/2$ and $\int_0^{D_1T_h} i_L dt$ is the gray area in Fig. 11. Consider the same output power, these gray areas are compared in Fig. 12, and the case in Fig. 11(b) has the minimum current stress. For any operating points in Mode 1 when $i_L(0) > 0$ or $i_L(0) < 0$, there always exists a corresponding case with $i_L(0) = 0$ to output the same power but with lower current stress. Therefore, the optimal operating condition in Mode 1 must be the case with $i_L(0) = 0$ in Fig. 11(b).

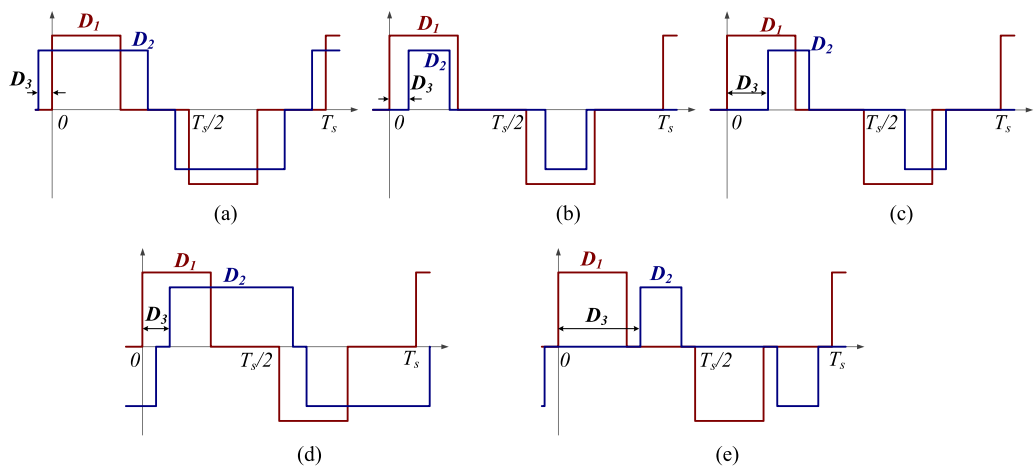

Fig. 8. Five different operation modes in the forward/buck scenario. (a) Mode 1: $D_3 \leq 0$. (b) Mode 2: $0 \leq D_3 \leq D_1$, $D_2 + D_3 \leq D_1$. (c) Mode 3: $0 \leq D_3 \leq D_1$, $D_2 + D_3 \geq D_1$. (d) Mode 4: $0 \leq D_3 \leq D_1$, $D_2 + D_3 \geq 1$. (e) Mode 5: $D_3 \geq D_1$.

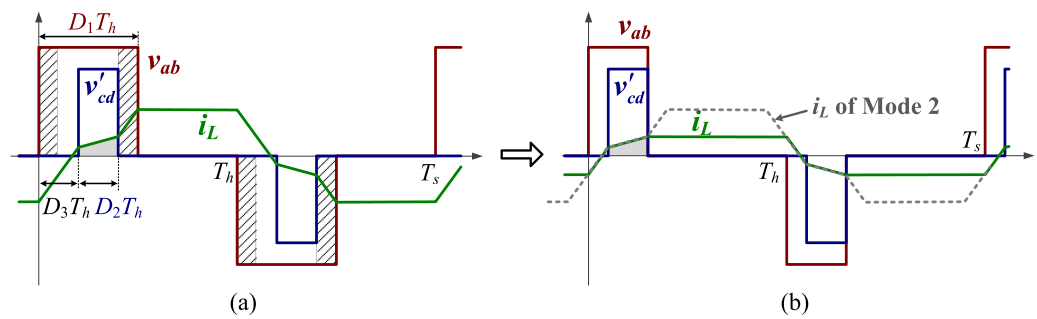

Fig. 9. Equivalence of Mode 2 to Mode 3.

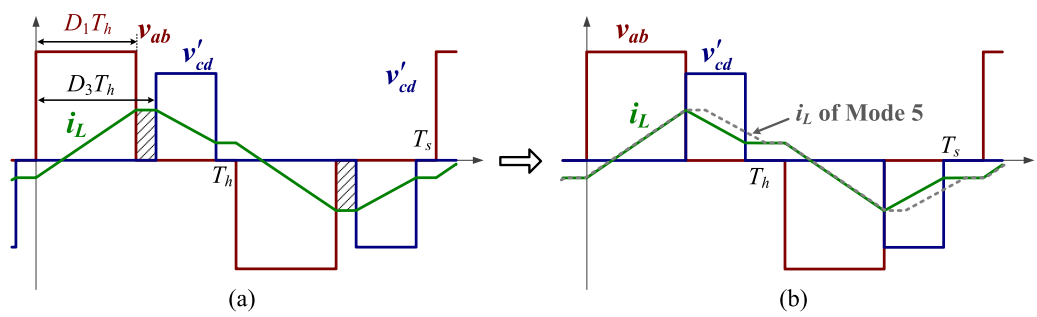

Fig. 10. Equivalence of Mode 5 to Mode 3.

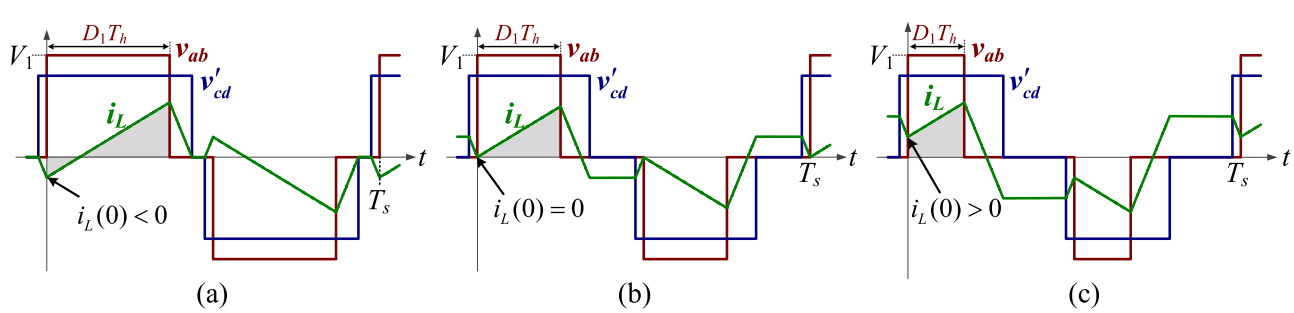

Fig. 11. Three different cases in Mode 1.

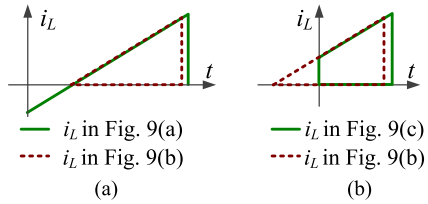

Fig. 12. Current-stress comparison of Mode 1 in different cases (the same output power).

Shrink of v'_{cd} at the rising and falling edges of v'_{cd} in Fig. 11(b) with a period $|D_3T_h|$ can let the DAB operate in Mode 3, as shown Fig. 13. This transformation does not change the output power and current stress, but the RMS value of i_L is reduced, and, hence, resulting in lower power losses. For the same reason as that in Modes 2 and 5, no further analysis is required for Mode 1.

From the aforementioned analysis, each operating point of Modes 1, 2, and 5 can be mapped into that of Mode 3 with a lower i_L RMS value; hence, the optimal operating conditions must not in Modes 1, 2, or 5, and detailed analysis of only Modes 3 and 4 is required.

V. Optimal Values of D_1, D_2, and D_3 in Mode 3

This section first derives the output power P and current stress I_{s3} of a DAB operating in Mode 3, then obtains the optimal operating conditions.

Fig. 14 depicts representative waveforms for v_{ab}, v'_{cd}, and i_L, where $0 \le D_3 \le D_1, D_2 + D_3 \ge D_1$, $-I_{o3}$ is the current at time 0, and I_{s3} is the current stress. Because of symmetrical operation, i_L changes from $-I_{o3}$ to I_{o3} over half a switching cycle

$$-I_{o3} + \frac{V_1 D_1 T_h - dV_1 D_2 T_h}{L} = I_{o3}. \tag{8}$$

The current stress I_{s3} can be calculated as

$$\begin{aligned} I_{s3} &= I_{o3} + \frac{dV_1}{L}(D_2 + D_3 - D_1)T_h \\ &= \frac{V_1}{4fL}((1-2d)D_1 + dD_2 + 2dD_3) \end{aligned} \tag{9}$$

where the switching frequency $f = 1/T_s$. The output power of the DAB in Mode 3 can be calculated as

$$P = V_1 \int_0^{D_1 T_h} i_L dt = \frac{dV_1^2}{4fL}(D_1 D_2 + 2D_1 D_3 - D_1^2 - D_3^2). \tag{10}$$

The aforementioned calculations can be easily performed with the assistance of Mathematica or any other similar software. To simplify the analysis, I_{s3} in (9) and P in (10) are normalized as

$$\begin{cases} I_{n3} = I_{s3}/I_b, I_b = \dfrac{V_1}{4fL} \\ P_n = P/P_b, P_b = \dfrac{dV_1^2}{2fL}. \end{cases} \tag{11}$$

On the basis of (9) and (10), we will express the current stress I_{n3} in terms of P_n. D_2 can be expressed as follows according to (10) and (11):

$$D_2 = \frac{(D_1 - D_3)^2 + 2P_n}{D_1}. \tag{12}$$

Substituting (12) into (9) and considering (11), one obtains

$$I_{n3} = (1-d)D_1 + \frac{2dP_n}{D_1} + \frac{dD_3^2}{D_1} \tag{13}$$

where D_1 and D_3 are constrained as shown in Fig. 8(c). The problem is to find the optimal values of D_1 and D_3 for a given P_n.

The partial derivative of I_{n3} with respect to D_3 can be expressed as

$$\begin{cases} \dfrac{\partial I_{n3}}{\partial D_3} = \dfrac{2dD_3}{D_1} \\ \dfrac{\partial^2 I_{n3}}{\partial D_3^2} = \dfrac{2d}{D_1} > 0. \end{cases} \tag{14}$$

I_{s3} is a convex function of D_3; hence, $\partial I_{n3}/\partial D_3 = 0$ can achieve a minimum I_{s3}, and we can obtain $D_3 = 0$. Then, (13) is simplified as

$$I_{s3} = (1-d)D_1 + \frac{2dP_n}{D_1}. \tag{15}$$

There is a certain range for D_1 under different P_n. Substituting $D_3 = 0$ into (12) and considering $0 < D_2 \le 0$, the range of D_1 in Mode 3 can be calculated as

$$\frac{1 - \sqrt{1 - 8P_n}}{2} \le D_1 \le \frac{1 + \sqrt{1 - 8P_n}}{2}. \tag{16}$$

We now can get the value of D_1 to achieve the minimum I_{s3}. Let $\partial I_{n3}/\partial D_1 = 0$, we obtain

$$D_1 = \sqrt{\frac{2dP_n}{1-d}} \triangleq \hat{D}_{1_c}. \tag{17}$$

When $\hat{D}_{1_c}$ is within the range of (16), i.e.,

$$\frac{1 - \sqrt{1 - 8P_n}}{2} \le \hat{D}_{1_c} \le \frac{1 + \sqrt{1 - 8P_n}}{2} \Rightarrow P_n \le \frac{d(1-d)}{2} \tag{18}$$

the minimum current stress is achieved when $D_1 = \hat{D}_{1_c}$, and D_2 can be calculated as $D_2 = D_1/d$ according to (12). Fig. 15 shows typical waveforms satisfy this condition, which is actually the so-called triangular operating mode.

While $\hat{D}_{1_c}$ is out of the range of (16), i.e., $P_n > d(1-d)/2$, the lowest stress is achieved when D_1 equals to the boundary value shown in (16). According to (15), when $0 < d \le 0.5$, $\hat{D}_{1_c} \ge (1 - \sqrt{1 - 8P_n})/2$; while $0.5 \le d < 1$, $\hat{D}_{1_c} > (1 - \sqrt{1 - 8P_n})/2$. To get the minimum value for I_{s3}, we should choose a D_1 close to $\hat{D}_{1_c}$ as follows:

$$D_1 = \begin{cases} \dfrac{1}{2}\left(1 - \sqrt{1 - 8P_n}\right), d \in (0, 0.5] \\ \dfrac{1}{2}\left(1 + \sqrt{1 - 8P_n}\right), d \in (0.5, 1). \end{cases} \tag{19}$$

In both cases, we can calculate that $D_2 = 1$.

Table II summarizes the conditions to achieve the minimum current stress for a DAB operating in Mode 3.

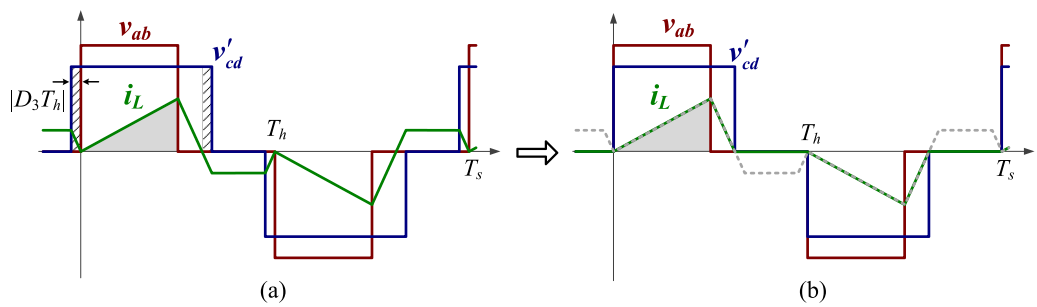

Fig. 13. Equivalence of Mode 1 to Mode 3.

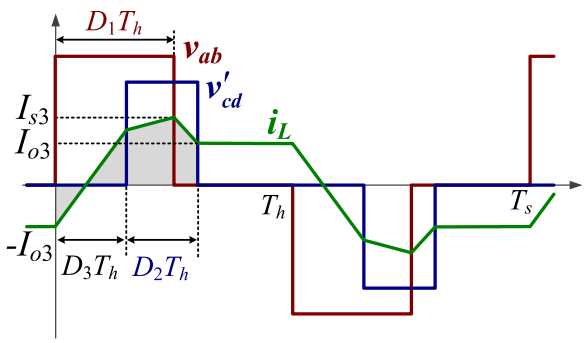

Fig. 14. Typical waveforms of the DAB in Mode 3.

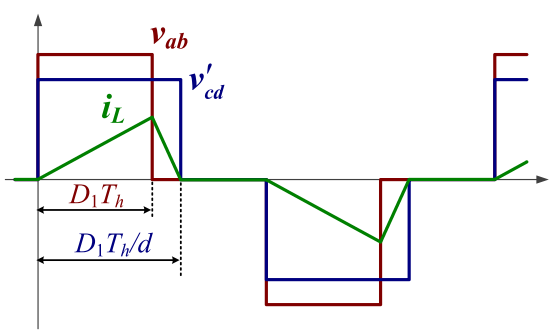

Fig. 15. Triangular operating mode.

TABLE II
CONDITIONS TO ACHIEVE THE MINIMUM i_L STRESS IN MODE 3

	$0 < P_n \leq \frac{d(1-d)}{2}$	$\frac{d(1-d)}{2} < P_n \leq 1/8$
D_1	$\sqrt{\frac{2dP_n}{1-d}}$	$\frac{1}{2}(1 \pm \sqrt{1-8P_n})$
D_2	D_1/d	1
D_3	0	0

VI. OPTIMAL VALUES OF D_1, D_2, AND D_3 IN MODE 4

This section derives the conditions to achieve the minimum stress of i_L for a DAB operating in Mode 4 shown in Fig. 16. The normalized output power P_n and current stress I_{n4} can be

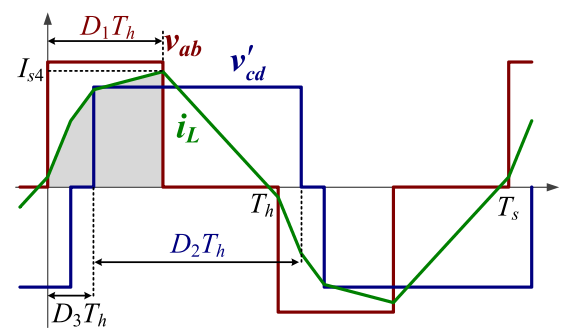

Fig. 16. Typical waveforms of the DAB in Mode 4.

derived similarly as for Mode 3 as follows:

$$P_n = \frac{4D_f - 4D_f^2 - (1-D_1)^2 - (1-D_2)^2}{4} \tag{20}$$

$$I_{n4} = (1-2d)D_1 + dD_2 + 2dD_3 = (1-d)D_1 + 2dD_f. \tag{21}$$

The relation between the output power, voltage gain, and current stress in Mode 4 can be obtained on the basis of (20) and (21). We can rewrite (20) as

$$D_f = \frac{1}{2}\left(1 - \sqrt{1-(1-D_1)^2-(1-D_2)^2-4P_n}\right). \tag{22}$$

Substituting D_f from (22) into (21) yields

$$I_{n4} = d + (1-d)D_1 - d\sqrt{1-(1-D_1)^2-(1-D_2)^2-4P_n}. \tag{23}$$

For a given output power P_n, we can choose D_1 and D_2 to minimize the current stress I_{n4}. Because $\partial I_{n4}/\partial D_2 < 0$ for $D_2 \in (0, 1]$, to get the minimum I_{n4} we should let $D_2 = 1$. Then, (23) can be simplified as

$$I_{n4} = d + (1-d)D_1 - d\sqrt{1-(1-D_1)^2-4P_n}. \tag{24}$$

There is a certain constraint on D_1 under different P_n. Combining (5) and (22) and considering $D_2 = 1$ and $D_3 \geq 0$, we obtain

$$D_1^2 - D_1 + 2P_n \geq 0. \tag{25}$$

TABLE III
CONDITIONS TO ACHIEVE THE MINIMUM STRESS OF i_L IN MODE 4

	$0 \le P_n \le \frac{d(1-d)}{2}$	$\frac{d(1-d)}{2} < P_n$
D_1	$\frac{1}{2}\left(1 \pm \sqrt{1-8P_n}\right)$	$1-(1-d)\sqrt{\frac{1-4P_n}{1-2d+2d^2}}$
D_2	1	1
D_3	0	$\frac{D_1-d}{2(1-d)}$

When $P_n \ge 1/8$, the condition (25) is satisfied for all D_1; when $0 \le P_n < 1/8$, the range of D_1 is calculated as

$$D_1 \in \left(0, \frac{1}{2}\left(1-\sqrt{1-8P_n}\right)\right] \cup \left[\frac{1}{2}\left(1+\sqrt{1-8P_n}\right), 1\right]. \tag{26}$$

To obtain the minimum stress of i_L in Mode 4, let $dI_{n4}/dD_1 = 0$. We can obtain the extrema of I_{n4} in (24) as

$$D_1 = 1-(1-d)\sqrt{\frac{1-4P_n}{1-2d+2d^2}} \triangleq \hat{D}_{1_d} \tag{27}$$

I_{n4} is a convex function because of the following:

$$\frac{\partial^2 I_{n4}}{dD_1^2} = \frac{d(1-D_1)^2}{(2D_1-D_1^2-4P_n)^{3/2}} + \frac{d}{\sqrt{2D_1-D_1^2-4P_n}} > 0. \tag{28}$$

When $\hat{D}_{1_d}$ is within the range obtained in (26), where $P_n \ge d(1-d)/2$, the condition to achieve the minimum stress of i_L is $D_1 = \hat{D}_{1_d}$, and D_3 can be calculated as

$$D_3 = \frac{1}{2}\left(1-\sqrt{\frac{1-4P_n}{1-2d+2d^2}}\right) = \frac{D_1-d.}{2(1-d)}. \tag{29}$$

When D_{1o} is out of the range obtained in (26), in which case $0 < P_n \le d(1-d)/2$, the minimum current stress is achieved when $D_1 = (1-\sqrt{1-8P_n})/2$ or $(1+\sqrt{1-8P_n})/2$, because I_{n4} with respect to D_1 is a convex function calculated in (28). In both cases, we obtain

$$D_1^2 - D_1 + 2P_n = 0. \tag{30}$$

Substituting P_n from (30) into (24) yields

$$I_{n4} = d + (1-2d)D_1. \tag{31}$$

Thus, to achieve the minimum value of I_{n4}, we should have

$$D_1 = \begin{cases} \frac{1}{2}\left(1-\sqrt{1-8P_n}\right), d \in (0, 0.5] \\ \frac{1}{2}\left(1+\sqrt{1-8P_n}\right), d \in (0.5, 1) \end{cases} \tag{32}$$

which is the same as that obtained in (19). In both cases, we can calculate $D_3 = 0$. Considering $D_2 = 1$, this condition is a boundary condition for Modes 3 and 4. Table III has summarized the minimum stress condition for Mode 4.

TABLE IV
OPTIMAL PHASE-SHIFT RATIOS IN FORWARD/BUCK SCENARIO

Condition	$0 \le P_n \le \frac{d(1-d)}{2}$	$\frac{d(1-d)}{2} < P_n$
D_1	$\sqrt{\frac{2dP_n}{1-d}}$	$1-(1-d)\sqrt{\frac{1-4P_n}{1-2d+2d^2}}$
D_2	D_1/d	1
D_3	0	$\frac{D_1-d}{2(1-d)}$

TABLE V
OPTIMAL PHASE-SHIFT RATIOS WHEN $P > 0$ (FORWARD)

Voltage gain	Power range	Optimal control parameters
$d < 1$	$P_n \in [0, \frac{d(1-d)}{2}]$	$D_1 = \sqrt{\frac{2dP_n}{1-d}}$, $D_2 = \frac{D_1}{d}, D_3 = 0$
	$P_n \in [\frac{d(1-d)}{2}, \frac{1}{4}]$	$D_1 = 1-(1-d)\sqrt{\frac{1-4P_n}{1-2d+2d^2}}$, $D_2 = 1, D_3 = \frac{D_1-d}{2(1-d)}$
$d > 1$	$P_n \in [0, \frac{d-1}{2d^2}]$	$D_2 = \sqrt{\frac{2P_n}{d-1}}$, $D_1 = dD_2, D_3 = dD_2 - D_2$
	$P_n \in [\frac{d-1}{2d^2}, \frac{1}{4}]$	$D_2 = 1-(d-1)\sqrt{\frac{1-4P_n}{d^2-2d+2}}$, $D_1 = 1, D_3 = \frac{(2-d)D_2+2d-3}{2(d-1)}$
$d = 1$	$P_n \in [0, \frac{1}{4}]$	$D_1 = D_2 = 1$, $D_3 = \frac{1-\sqrt{1-4P_n}}{2}$

VII. GLOBAL OPTIMAL PHASE-SHIFT RATIOS

A. Optimal Phase-Shift Ratios in Forward/Buck Scenario

According to Section IV, for any operating points in Modes 1, 2, or 5, there always exists a corresponding point in Mode 3 with the same output power and current stress, but with lower power losses; thus, the optimal operating points must lie in Mode(s) 3 or/and 4. In Sections V and VI, we have derived the optimal values of D_1, D_2, and D_3 for Modes 3 and 4 listed in Tables II and III, respectively.

Consider a DAB with output power $P_n \le d(1-d)/2$; it can operate in either Mode 3 or 4 on the basis of the aforementioned analysis. If it operates in Mode 4, the optimal phase-shift ratios are shown in the gray column of Table III where $D_2 = 1, D_3 = 0$, and this condition is also in Mode 3 according to Fig. 8(c). Therefore, when $P_n \le d(1-d)/2$, the optimal condition must be in Mode 3. Similarly, when $d(1-d)/2 < P_n \le 1/4$, the optimal condition must be in Mode 4. Combine the white column of Tables II and III, we obtain the conditions to achieve the minimum stress of i_L when $P_n > 0, d < 1$, as shown in Table IV.

B. Optimal Phase-Shift Ratios When $d = 1$

The optimal values of D_1, D_2, and D_3 when $d = 1$ can be derived from Table IV. Considering the case in which

TABLE VI
OPTIMAL PHASE-SHIFT RATIOS WHEN $P < 0$ (BACKWARD)

Voltage gain	Power range	Optimal control parameters
$d < 1$	$P_n \in [-\frac{d(1-d)}{2}, 0]$	$D_1 = \sqrt{-\frac{2dP_n}{1-d}}$, $D_2 = \frac{D_1}{d}, D_3 = D_1 - \frac{D_1}{d}$
	$P_n \in [-\frac{1}{4}, -\frac{d(1-d)}{2}]$	$D_1 = 1-(1-d)\sqrt{\frac{1+4P_n}{1-2d+2d^2}}$, $D_2 = 1, D_3 = -\frac{(2d-1)D_1+2-3d}{2(1-d)}$
$d > 1$	$P_n \in [-\frac{d-1}{2d^2}, 0]$	$D_2 = \sqrt{-\frac{2P_n}{d-1}}$, $D_1 = \frac{D_2}{d}, D_3 = 0$
	$P_n \in [-\frac{1}{4}, -\frac{d-1}{2d^2}]$	$D_2 = 1-(d-1)\sqrt{\frac{1+4P_n}{d^2-2d+2}}$, $D_1 = 1, D_3 = \frac{1-dD_2}{2(d-1)}$
$d = 1$	$P_n \in [-\frac{1}{4}, 0]$	$D_1 = D_2 = 1$, $D_3 = \frac{\sqrt{1+4P_n}-1}{2}$

TABLE VII
GLOBAL OPTIMAL PHASE-SHIFT RATIOS

Voltage gain	D_f range	Optimal control parameters
$d \le 0.95$	$D_f \in (\frac{1-d}{2}, \frac{1}{2}]$	$D_1 = 1 - \frac{(1-d)(1-2D_f)}{d}, D_2 = 1$
	$D_f \in [0, \frac{1-d}{2}]$	$D_1 = \frac{2d}{1-d}D_f, D_2 = \frac{2}{1-d}D_f$
	$D_f \in [-\frac{1-d}{2}, 0)$	$D_1 = -\frac{2d}{1-d}D_f, D_2 = -\frac{2}{1-d}D_f$
	$D_f \in [-\frac{1}{2}, -\frac{1-d}{2})$	$D_1 = 1 - \frac{(1+2D_f)(1-d)}{d}, D_2 = 1$
$d \ge 1.05$	$D_f \in (\frac{d-1}{2d}, \frac{1}{2}]$	$D_1 = 1, D_2 = 2-d+2(d-1)D_f$
	$D_f \in [0, \frac{d-1}{2d}]$	$D_1 = \frac{2d}{d-1}D_f, D_2 = \frac{2}{d-1}D_f$
	$D_f \in [-\frac{d-1}{2d}, 0)$	$D_1 = -\frac{2d}{d-1}D_f, D_2 = -\frac{2}{d-1}D_f$
	$D_f \in [-\frac{1}{2}, -\frac{d-1}{2d})$	$D_1 = 1, D_2 = 2-d+2(1-d)D_f$
$0.95 < d < 1.05$	$D_f \in [-\frac{1}{2}, \frac{1}{2}]$	$D_1 = 1, D_2 = 1$

$P_n > 0, d = 1$, we obtain $d(1-d)/2 = 0$; therefore, the optimal phase-shift ratios must be the second column of Table IV: For $P_n > 0, D_1 = 1, D_2 = 1$, and D_3 can be calculated according to (29) to yield

$$D_3 = 1 - \sqrt{1-4P_n}/2. \tag{33}$$

C. Global Optimal Phase-Shift Ratios

On the basis of the results in Table IV and (33), the optimal phase-shift ratios of other scenarios such as forward/boost, backward/buck, and backward/boost can be obtained using the equivalence introduced in Section II. For example, the optimal values of D_1, D_2, and D_3 of forward/boost scenario can be derived by substituting (4) into Table IV. The global optimal phase-shift ratios are presented in Tables V and VI.

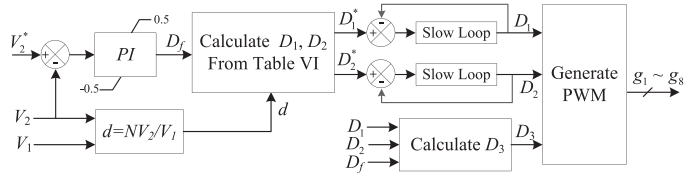

Fig. 17. Control scheme to achieve the minimum stress of the inductor current [18].

TABLE VIII
CIRCUIT PARAMETERS USED IN THE EXPERIMENTS

V_1 DC voltage 1	$150 \sim 300$ V
V_2 DC voltage 2	120 V
N Transformer turns ratio	2:1
f Switching frequency	40 kHz
L_1 Inductor	90 μH
C_1 DC capacitor 1	1.1 mF
C_2 DC Capacitor 2	3 mF
MOSFET	IPW65R037C6

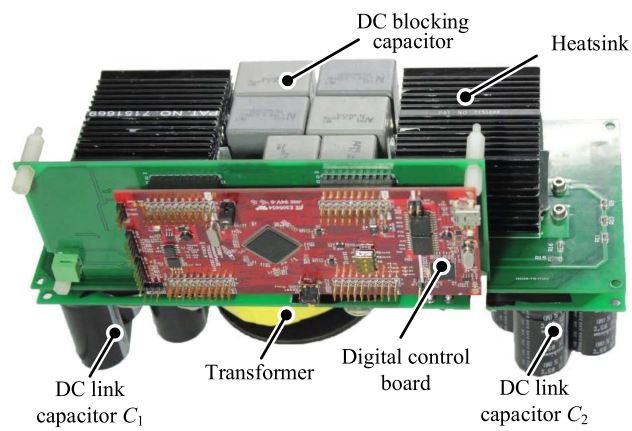

Fig. 18. DAB prototype.

VIII. CONTROL FOR GLOBAL MINIMUM REACTIVE POWER

This section presents a DAB control scheme to regulate the output voltage with minimum reactive power.

D_f is chosen to regulate the output voltage because D_f is always positively correlated to the output power when $D_f \in [-1/2, 1/2]$ according to (6), and this is not the case for D_1, D_2, or D_3: $D_1, D_2 \in [0, 1]$, and D_3 is always 0 in Mode 3.

In steady state, the optimal operating modes can be indicated using D_f and d. Consider the case in which $P_n > 0, d < 1$ in Table V. When $P_n \in (0, d(1-d)/2]$, on the basis of (5) and Table V, D_f and D_1 can be re-written as

$$\begin{cases} D_f = \sqrt{\frac{(1-d)P_n}{2d}} \in \left(0, \frac{1-d}{2}\right] \\ D_1 = \frac{2dD_f}{1-d} \\ D_1 = \frac{2D_f}{1-d}. \end{cases} \tag{34}$$

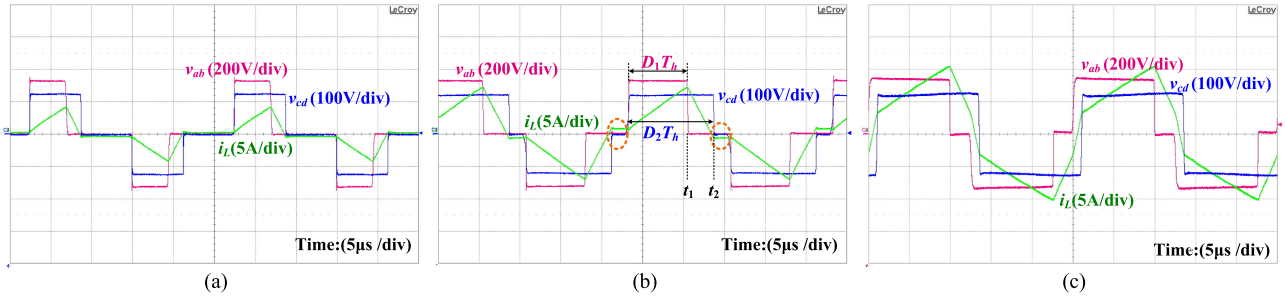

Fig. 19. Experimental waveforms of the prototype modulated using the proposed TPS when $d = 0.75$.

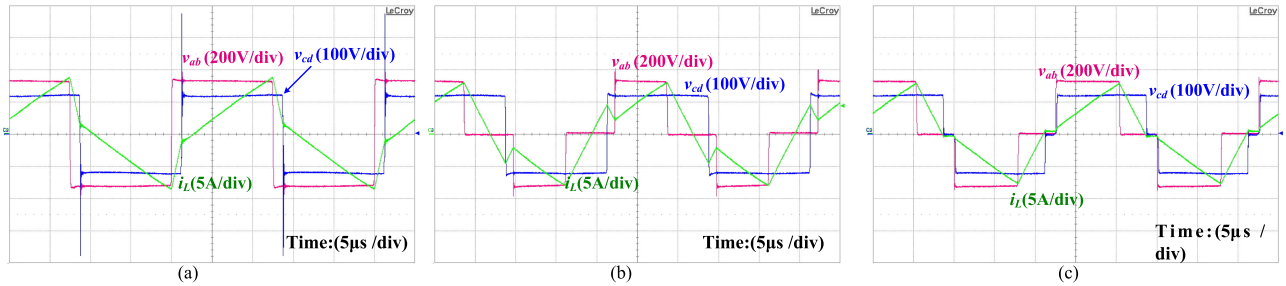

Fig. 20. Experimental waveforms using SPS, FDM, and TPS, when $d = 0.75$ and $P = 850$ W.

Similarly, while $P_n \in (d(1-d)/2, 1/4]$, D_f and D_1 can be expressed as

$$\begin{cases} D_f = \dfrac{1}{2}\left(1 - d\sqrt{\dfrac{1-4P_n}{1-2d+2d^2}}\right) \in \left(\dfrac{1-d}{2}, \dfrac{1}{2}\right] \\ D_1 = 1 - \dfrac{(1-d)(1-2D_f)}{d}, D_2 = 1. \end{cases} \tag{35}$$

Being monotonically related to P_n, D_f can be used to differentiate between the modes. When $D_f \in (0, (1-d)/2]$ and $((1-d)/2, 1/2]$, the optimal values of D_1 and D_2 can be calculated using D_f and d according to (34) and (35), which is convenient for control implementation. Similar calculations can be performed for other conditions based on Tables V and VI, and the results are presented in Table VII, where the operating modes are differentiated using D_f and d.

In Table VII, when d is close to 1, the boundary D_f including $(1-d)/2$ and $(d-1)/(2d)$ will be close to 0. As a result, the DAB may frequently transit between different modes, thereby affecting stability. To circumvent this difficulty, the DAB is modulated using SPS when d is close to 1, and in this paper when $d \in (0.95, 1.05)$, SPS is employed, as shown in Table VII (other range of d can also be used). Within this range, the reactive power is small anyway as v_{ab} and v'_{cd} have similar amplitudes.

Fig. 17 shows the control scheme [18]. The secondary side dc-bus voltage V_2 is compared with its reference V_2^* to generate the voltage error, and D_f is obtained using a PI compensator. D_f is limited in the range $[-0.5, 0.5]$ to ensure a monotonic relation between D_f and output power. V_1 and V_2 are used to calculate the voltage gain. D_f and d together decide D_1^* and D_2^* according to Table VII, where D_1^* and D_2^* are the reference values of D_1 and D_2, respectively. Slow loops are used to generate actual D_1 and D_2 to avoid influence of the mode-selection on dynamic response. D_3 is calculated on the basis of (5). Finally, gate signals $g_1 \sim g_8$ are generated from D_1, D_2, and D_3.

IX. Experimental Results

A DAB prototype with parameters listed in Table VIII, is used to confirm the presented analysis. A TI LAUNCHXL-F28377S kit is employed to control the DAB. Fig. 18 shows the photograph of the prototype.

Fig. 19 shows the experimental waveforms of the prototype modulated using the proposed TPS when $d = 0.75$. In Fig. 19(a) and (b) where the power is smaller than $d(1-d)P_b/2 = 1$ kW [see Table IV and (11)], the DAB operates in triangular mode with $D_2 \approx dD_1, D_3 = 0$, as predicted by the first column of Table IV; in Fig. 19(c) where $P > 1$ kW, the waveforms follow the prediction of the second column of Table IV with $D_2 = 1$. Note that in Fig. 19(b), during the period marked by the dotted circle, $i_L \neq 0$, which is different from Fig. 15, and this difference is caused by the phase drift [24]: $i_L(t_1)$ is greater than $i_L(t_2)$; at t_2, it takes longer time to charge and discharge the capacitance of power switches, as a result, the actual $D_2 > dD_1$.

For comparison, the DAB modulated using SPS and frequency-division multiplexing (FDM) [14] are also tested. FDM is a representative control scheme derived using frequency domain analysis with detailed implementation guidance and is therefore chosen to compare with the proposed TPS derived using the time domain analysis.

Fig. 20 shows the experimental waveforms using three different modulation methods when $d = 0.75$, $P = 850$ W, where the current stresses of i_L using SPS, FDM, and TPS are 8.75, 8.04, and 7.84 A, respectively. In Fig. 20(c), i_L becomes triangular in

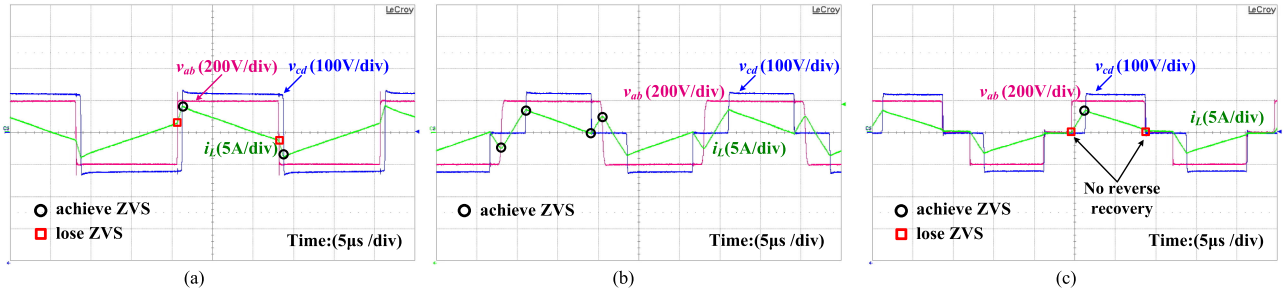

Fig. 21. Experimental waveforms using SPS, FDM, and TPS, when $d = 1.25$, and $P = 250$ W.

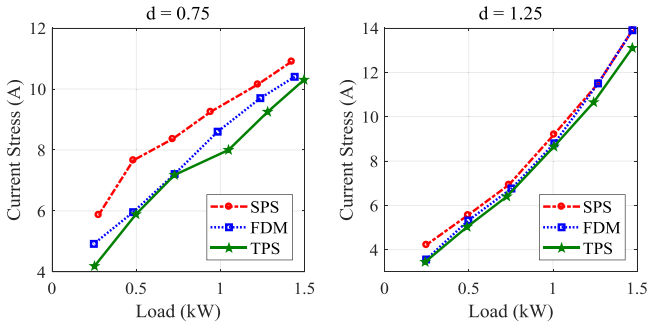

Fig. 22. Current stress of the DAB prototype using SPS, FDM, and TPS.

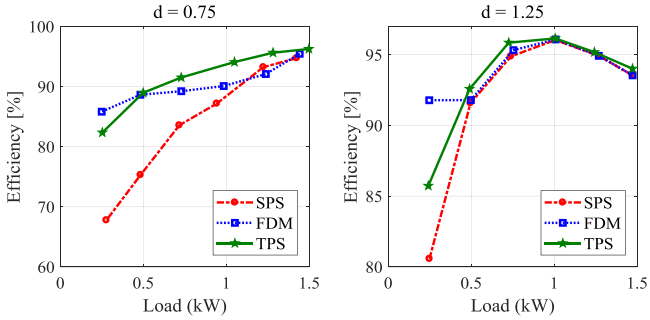

Fig. 23. Efficiency comparison of the DAB prototype using SPS, FDM, and TPS.

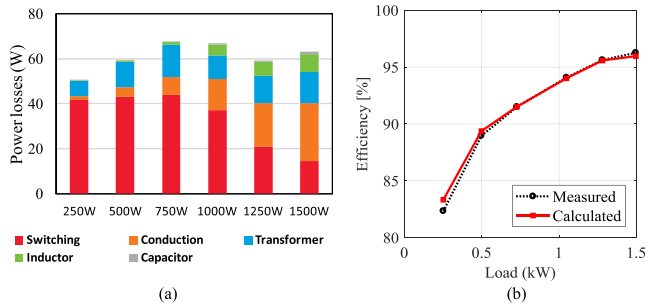

Fig. 24. (a) Calculated power losses' breakdown when $d = 0.75$. (b) Calculated and measured efficiency.

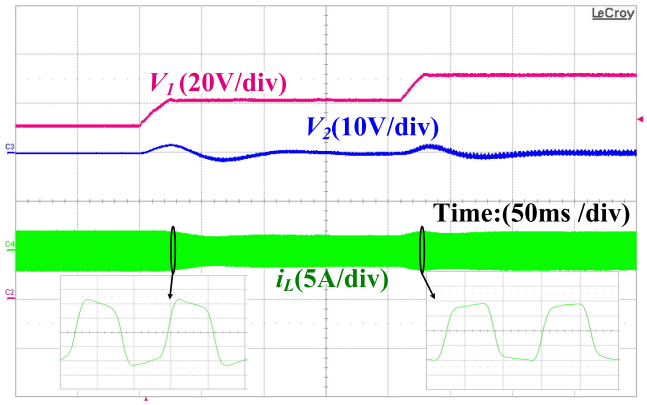

Fig. 25. Mode-Transition-Test waveforms.

shape, indicating $D_3 = 0$, $D_1 = dD_2$, which is in accordance with Table II. Fig. 21 shows the experimental waveforms under $d = 1.25, P = 0.25$ kW, where the current stresses using SPS, FDM, and TPS are 4.22, 3.56, and 3.45 A, respectively. In Fig. 21(c), $D_2 = 1$, which is in accordance with Table III. Fig. 22 plots the current stress when $d = 0.75$ and 1.25; the DAB modulated using the proposed TPS has the minimum current stress (hence the minimum reactive power) under different load conditions. These experimental results verify that D_1, D_2, and D_3 given in Table VII can achieve minimum reactive power.

Fig. 23 compares the efficiency of the DAB prototype modulated using SPS, FDM, and TPS, where V_2 is regulated at 120 V, and $V_1 = 320$ V when $d = 0.75$, and $V_1 = 192$ when $d = 1.25$. TPS can achieve the highest efficiency in the load range of 33% to 100% both when $d = 0.75$ and 1.25. Under light load conditions (<33% load), the efficiency of TPS is lower than that of FDM. In this load range, when using FDM modulation, all the power devices can achieve ZVS-ON as shown in Fig. 21(b); while using the proposed TPS shown in Fig. 21(c), only two devices achieve ZVS and other six devices switch when $i_L = 0$. Although the crossover losses in the MOSFET (v_{ds} and i_L overlap) and diode's reverse-recovery losses have been avoided, yet the energy stored in C_{ds} in these devices is dissipated (similar to the critical current mode). This is verified by the breakdown of power losses in Fig. 24, where switching loss is the main contributor to the overall losses under light conditions. For this reason, the proposed method is more suitable for the high-power applications where the major power loss is conduction loss such as a PET. To achieve both optimal switching and conduction losses, the phase-shift ratios can be slightly adjusted on the basis of this paper, such that the inductor current is equal to a predefined value at the switching instant that can charge/discharge

the parasitic capacitance of switches during dead time, similar to [25].

Experiments have been performed to test mode-transition performance. Fig. 25 shows the experimental waveforms when d changes from 1.14 to 1, then to 0.89. The output voltages V_2 have some overshoot during the transition, which are however acceptable.

X. Conclusion

This paper presented a simplified derivation of optimal phase-shift ratios to achieve the global minimum reactive power and minimum current stress in a DAB. We first introduced a transformation that different DAB operating scenarios (forward/backward, buck/boost) can be equivalent to one another, then only optimization of one scenario (forward/buck) is required, and the optimal phase-shift ratios of other scenarios can be obtained using this equivalence. For the forward/buck scenario, there are five different operating modes (Modes 1–5). Using a graphical method, this paper proves that each operating point of Modes 1, 2, and 5 can be mapped into that of Mode 3 with lower conduction losses, and that only two modes require consideration. The optimization process of these two modes is derived in a step-by-step manner. These equivalences not only simplify the calculation but also provide better understanding for the DAB operating principle. Global optimal phase-shift ratios that minimize the reactive power under four different DAB operating scenarios (forward/backward, buck/boost) are presented. A table (see Table VII) and a control diagram are presented for the practical implementation to minimize DAB reactive power. Experimental results substantiated the analysis.

References

[1] R. W. de Doncker, D. M. Divan, and M. H. Kheraluwala, "A three-phase soft-switched high power density DC/DC converter for high power applications," in *Proc. Conf. Rec. IEEE Ind. Appl. Soc. Annu. Meeting*, Oct. 1988, vol. 1, pp. 796–805.

[2] R. W. A. A. de Doncker, D. M. Divan, and M. H. Kheraluwala, "A three-phase soft-switched high-power-density DC/DC converter for high-power applications," *IEEE Trans. Ind. Appl.*, vol. 27, no. 1, pp. 63–73, Jan. 1991.

[3] C. Mi, H. Bai, C. Wang, and S. Gargies, "Operation, design and control of dual H-bridge-based isolated bidirectional dc-dc converter," *IET Power Electron.*, vol. 1, no. 4, pp. 507–517, Dec. 2008.

[4] B. Zhao, Q. Song, W. Liu, G. Liu, and Y. Zhao, "Universal high-frequency-link characterization and practical fundamental-optimal strategy for dual-active-bridge dc-dc converter under PWM plus phase-shift control," *IEEE Trans. Power Electron.*, vol. 30, no. 12, pp. 6488–6494, Dec. 2015.

[5] K. Vangen, T. Melaa, S. Bergsmark, and R. Nilsen, "Efficient high-frequency soft-switched power converter with signal processor control," in *Proc. 13th Int. Telecommun. Energy Conf.*, Nov. 1991, pp. 631–639.

[6] K. Vangen, T. Melaa, and A. K. Adnanes, "Soft-Switched high-frequency, high power dc/ac converter with IGBT," in *Proc. 23rd Annu. IEEE Power Electron. Spec. Conf., Rec.*, Jun. 1992, vol. 1, pp. 26–33.

[7] G. G. Oggier, G. O. Garca, and A. R. Oliva, "Switching control strategy to minimize dual active bridge converter losses," *IEEE Trans. Power Electron.*, vol. 24, no. 7, pp. 1826–1838, Jul. 2009.

[8] B. Zhao, Q. Yu, and W. Sun, "Extended-phase-shift control of isolated bidirectional DC–DC converter for power distribution in microgrid," *IEEE Trans. Power Electron.*, vol. 27, no. 11, pp. 4667–4680, Nov. 2012.

[9] H. Bai and C. Mi, "Eliminate reactive power and increase system efficiency of isolated bidirectional dual-active-bridge DC–DC converters using novel dual-phase-shift control," *IEEE Trans. Power Electron.*, vol. 23, no. 6, pp. 2905–2914, Nov. 2008.

[10] B. Zhao, Q. Song, and W. Liu, "Power characterization of isolated bidirectional dual-active-bridge DC–DC converter with dual-phase-shift control," *IEEE Trans. Power Electron.*, vol. 27, no. 9, pp. 4172–4176, Sep. 2012.

[11] B. Zhao, Q. Song, and W. Liu, "Efficiency characterization and optimization of isolated bidirectional DC–DC converter based on dual-phase-shift control for DC distribution application," *IEEE Trans. Power Electron.*, vol. 28, no. 4, pp. 1711–1727, Apr. 2013.

[12] B. Zhao, Q. Song, W. Liu, and W. Sun, "Current-stress-optimized switching strategy of isolated bidirectional DC–DC converter with dual-phase-shift control," *IEEE Trans. Ind. Electron.*, vol. 60, no. 10, pp. 4458–4467, Oct. 2013.

[13] B. Zhao, Q. Song, W. Liu, G. Liu, and Y. Zhao, "Universal high-frequency-link characterization and practical fundamental-optimal strategy for dual-active-bridge dc-dc converter under PWM plus phase-shift control," *IEEE Trans. Power Electron.*, vol. 30, no. 12, pp. 6488–6494, Dec. 2015.

[14] W. Choi, K. M. Rho, and B. H. Cho, "Fundamental duty modulation of dual-active-bridge converter for wide-range operation," *IEEE Trans. Power Electron.*, vol. 31, no. 6, pp. 4048–4064, Jun. 2016.

[15] H. Shi, H. Wen, J. Chen, Y. Hu, L. Jiang, and G. Chen, "Minimum-reactive-power scheme of dual-active-bridge DC–DC converter with three-level modulated phase-shift control," *IEEE Trans. Ind. Appl.*, vol. 53, no. 6, pp. 5573–5586, Nov. 2017.

[16] F. Krismer and J. W. Kolar, "Closed form solution for minimum conduction loss modulation of DAB converters," *IEEE Trans. Power Electronics*, vol. 27, no. 1, pp. 174–188, Jan. 2012.

[17] A. K. Jain and R. Ayyanar, "PWM control of dual active bridge: Comprehensive analysis and experimental verification," *IEEE Trans. Power Electron.*, vol. 26, no. 4, pp. 1215–1227, Apr. 2011.

[18] J. Huang, Y. Wang, Z. Li, and W. Lei, "Unified triple-phase-shift control to minimize current stress and achieve full soft-switching of isolated bidirectional DC–DC converter," *IEEE Trans. Ind. Electron.*, vol. 63, no. 7, pp. 4169–4179, Jul. 2016.

[19] N. Hou, W. Song, and M. Wu, "Minimum-current-stress scheme of dual active bridge DC–DC converter with unified phase-shift control," *IEEE Trans. Power Electron.*, vol. 31, no. 12, pp. 8552–8561, Dec. 2016.

[20] A. Tong, L. Hang, G. Li, X. Jiang, and S. Gao, "Modeling and analysis of a dual-active-bridge-isolated bidirectional DC/DC converter to minimize RMS current with whole operating range," *IEEE Trans. Power Electron.*, vol. 33, no. 6, pp. 5302–5316, Jun. 2018.

[21] N. Schibli, "Symmetrical multilevel converters with two quadrant DC–DC feeding," Ph.D. dissertation, EPFL, Lausanne, Switzerland, 2000.

[22] F. Krismer, "Modeling and optimization of bidirectional dual active bridge DC–DC converter topologies," Ph.D. dissertation, ETH Zurich, Zurich, Switzerland, 2010.

[23] G. Xu, D. Sha, J. Zhang, and X. Liao, "Unified boundary trapezoidal modulation control utilizing fixed duty cycle compensation and magnetizing current design for dual active bridge DC–DC converter," *IEEE Trans. Power Electron.*, vol. 32, no. 3, pp. 2243–2252, Mar. 2017.

[24] J. Hiltunen, V. Visnen, R. Juntunen, and P. Silventoinen, "Variable-Frequency phase shift modulation of a dual active bridge converter," *IEEE Trans. Power Electron.*, vol. 30, no. 12, pp. 7138–7148, Dec. 2015.

[25] A. Taylor, G. Liu, H. Bai, A. Brown, P. M. Johnson, and M. McAmmond, "Multiple-phase-shift control for a dual active bridge to secure zero-voltage switching and enhance light-load performance," *IEEE Trans. Power Electron.*, vol. 33, no. 6, pp. 4584–4588, Jun. 2018.

Shuai Shao (M'17) was born in Hunan Province, China, in 1987. He received the B.S. degree from Zhejiang University, Hangzhou, China, in 2010, and the Ph.D. degree in electrical engineering from the University of Nottingham, Nottingham, U.K., in 2015.

In December 2015, he became a Lecturer with the College of Electrical Engineering, Zhejiang University. His research interests include solid state transformers, bi-directional dc–dc converters, and fault detection in power converters.

Mingming Jiang received the B.S. and M.S. degrees in electrical engineering from Zhejiang University, Hangzhou, China, in 2015 and 2018, respectively.

He is currently with Hangzhou EV-Tech, China. His research interests include power module design and bi-directional dc–dc converters.

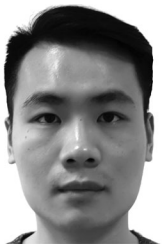

Weiwen Ye received the B.S. degree in electrical engineering from Hunan University, ChangSha, China, in 2017. He is currently working toward the M.S. degree at Zhejiang University, Hangzhou, China.

His research interests include bi-directional dc–dc converters and modular multi-level converters.

Yucen Li was born in Hubei, China, in 1995. He received the B.S. degree in electrical engineering from Zhejiang University, Hangzhou, China, in 2017. He is currently working toward the M.S. degree at the Department of Applied Electronics, Zhejiang University. His research interest focuses on high-efficiency dc/dc converters.

Junming Zhang (M'10–SM13) received the B.S., M.S., and Ph.D. degrees from Zhejiang University, Hangzhou, China, in 1996, 2000, and 2004, respectively, all in electrical engineering.

He is currently a Professor with the College of Electrical Engineering, Zhejiang University. From 2010 to 2011, he was a Visiting Scholar with the Department of Electrical and Computer Engineering, Michigan State University, East Lansing, MI, USA. His research interests include power electronics system integrations, power management, and high-efficiency converters.

Prof. Zhang is an Associate Editor for the IEEE TRANSACTIONS ON INDUSTRY APPLICATIONS and *CPSS Transactions on Power Electronics and Applications*.

Kuang Sheng (M'99–SM'08) received the B.Sc. degree from Zhejiang University, Hangzhou, China, in 1995, and the Ph.D. degree from Heriot-Watt University, Edinburgh, U.K., in 1999.

He is currently a Professor with Zhejiang University. His current research interests include all aspects of power semiconductor devices, and ICs on SiC and Si.